Check for updates

Surface charge dictates the mechanism of cellular uptake of fluorescent amine passivated carbon dots

Adryanne Clermont-Paquette,†[abc] Gianluca Fuoco,†[b] Cécilia R. Brancheriau,[c] Alisa Piekny*[c] and Rafik Naccache [ID] *[ab]

The surface charge of carbon dots (CDs) governs cellular uptake; however, studies seldom compare CDs with similar physico-chemical properties thereby introducing confounding variables. Here, we investigate how the surface charge of amine-passivated carbon dots with similar optical and chemical properties influences their uptake in human cells. We synthesized CDs using citric acid diethylenetriamine (DT3) or pentaethylenehexamine (PH6) using microwave-assisted synthesis. Extensive characterization confirmed their physico-chemical and optical properties. Ion exchange column chromatography was used to separate CDs into fractions with surface charges ranging from −35 mV to +7 mV, which were then added to HeLa cells. FT-IR analysis shows a visible increase of the amide stretch at 1646 cm^{-1} as charge decreases for the separated fractions revealing changes to surface functionalities. Fluorescence microscopy revealed a correlation between surface charge and cellular uptake. Our study shows a greater uptake of DT3-CDs by 1.17-fold with a surface charge of −14 mV, which were also enriched in the cytosol by 4.12-fold, compared to those with a charge of −35 mV, which localized at the lysosomes which is in accordance with our previous study. In contrast, PH6-CDs remained consistent regardless of their charge (+7 mV *vs.* −6 mV), with a preference for lysosomes. This study reveals how surface charge and chemical composition of CDs impacts cellular uptake and localization. These findings show how CDs could be tailored for specific applications in bioimaging and nanomedicine.

Introduction

Carbon dots (CDs) have gained significant attention due to their remarkable optical properties and physico-chemical versatility. Researchers have harnessed these properties for diverse applications including photovoltaic solar cells, chemical catalysis, drug delivery systems and bioimaging probes.[1–15] CDs are quasi spherical fluorescent nanoparticles with diameters of ~10 nm.[16,17] They typically comprise an amorphous sp^2-conjugated aromatic carbon core with surfaces that can be decorated with a multitude of functional groups.[18–21] CDs may be synthesized from complex carbon sources such as orange juice or soya beans, or more precisely defined precursors such as citric acid, glucose and amino acids.[22–29]

The synthesis typically involves using hydrothermal/solvothermal routes, or microwave-assisted synthesis, which has gained popularity owing to shorter reaction times and lower energy requirements.[30–35] The chemical composition of the CD surface can be tailored *via* the precursors and passivating agents used during synthesis.[36–38] The latter contributes to forming an outer layer on the surfaces of the dots. The chemical composition of the passivation layer will comprise functional groups present in the passivating agents, which may include carboxyls, thiols and amines, among others, which often alter the optical properties of the CDs including changes in fluorescence quantum yields.[39–44] CD fluorescence remains a phenomenon which is not fully understood;[45] however, there are many theories that point towards a plausible explanation such as the quantum confinement effect and conjugated cores/heteroatom rich surface states mechanisms.[1,46,47] Amine passivation has been reported to confer ideal optical properties with high quantum yields typically reaching up to 80% (similar to fluorescent dyes).[26,48–52] This can be explained by how electron-donating passivating groups minimize non-emissive traps limiting non-radiative relaxation, which enhances the observed fluorescence quantum yield.[16] Higher quantum yields are typically attractive for bioimaging applications as less material may be needed to achieve a measurable optical response.

Currently, metal nanoclusters, dye-doped, lanthanide-doped nanoparticles, as well as quantum dots are being developed for use in bioimaging applications owing to their impressive optical properties. However, several challenges persist ascribed

[a]Department of Chemistry and Biochemistry and Center for NanoScience Research, Concordia University, Montreal, QC, H4B 1R6, Canada. E-mail: rafik.naccache@concordia.ca

[b]Quebec Centre for Advanced Materials, Department of Chemistry and Biochemistry, Concordia University, Montreal, QC, H4B 1R6, Canada

[c]Department of Biology and the Centre for Microscopy and Cellular Imaging, Concordia University, Montreal, QC, H4B 1R6, Canada

† These authors contributed equally to this work.

to poor photostability, low aqueous dispersibility and/or high cytotoxicity.[53–56] Amine passivated CDs offer a promising alternative that effectively mitigates these challenges, rendering them ideal for use as bioimaging probes.[35,57] However, how distinct physico-chemical properties affects their interaction with cells remains largely unclear.

Previous reports have shown that size, shape and surface functionality can all affect the cellular uptake and/or localization of nanoparticles in different cell types. Polymer nanoparticles have been shown to have size-dependent uptake patterns. Dawson and Halbert demonstrated that larger polymer nanoparticles are more readily taken up by Hep2 2B cells, in comparison to their counterparts.[58] Another report has shown that the shape of silica nanoparticles can affect cellular uptake. Rod and long rod-shaped silica nanoparticles were reported to enter human melanoma cells at faster rates compared to spherical-shaped silica nanoparticles.[59] In addition, surface functionalization also affects cellular uptake, as studies showed that adding polyethylene glycol (PEG) to nanoparticle surfaces decreases their uptake by mouse embryonic fibroblasts.[60]

Size, shape and surface functionality have also been shown to affect the endocytic capabilities of nanoparticles; however, these properties are seldom studied independently. Changing the shape of a rod-like nanoparticle to a sphere-like counterpart will most likely change their diameter and surface area. Adding polymers such as PEG, or PEI to the surface of nanoparticles would change their physico-chemical properties while also increasing their surface area.[61] As such, it is challenging to study the effect of one variable while keeping others constant. Amine passivated CDs synthesized by the Naccache group tend to be small and very similar in size (2 nm in diameter), varying by ±0.50 nm. Therefore, modifications are not predicted to dramatically affect their size and alter the mechanism of cellular uptake. Typically, clathrin mediated endocytosis is the predominant form of endocytosis for particles of less than 200 nm in diameter.[62]

The surface charge of nanoparticles can affect their cellular uptake. Ronzani showed that surface charges of CDs change with passivating agents that differ in their amine content. Using four passivating agents with increasing amine content, four types of CDs were synthesized with a corresponding increase in positive surface charge. When added to human macrophages, the CDs showed a positive relationship between increasing surface charge and cellular uptake.[63] Another report compared the cellular uptake of CDs synthesized using bovine serum albumin, which had positive surface charge with CDs synthesized using citric acid, which had negative surface charge. They found that the negatively charged CDs were more easily taken up by mouse macrophages as opposed to the positively charged CDs.[64] However, while previous studies have shown how surface charge can affect cellular uptake, these studies were not performed with chemically comparable CDs, which could impart differences in cellular uptake and localization. Indeed, synthesis of CDs from distinct precursors introduces numerous confounding variables due to differences in their physical and chemical composition.

While CDs have ideal optical properties for bioimaging, it is not clear how they enter and/or localize in cells. Elucidating the properties that confer mechanisms of uptake would pave the way for designing nanoparticles for targeted bioimaging applications.[1]

Herein, we investigated how the surface charge of CDs bearing similar chemical properties impacts their are able to clearly demonstrate that even small charge uptake and localization in human cells. To achieve this we synthesized CDs from citric acid and diethylenetriamine (DT3), or pentaethylenehexamine (PH6) precursors maintaining the same synthesis conditions and precursors, while separating them based on their surface charge using anion exchange column chromatography. This approach ensured that any observed differences in cellular uptake arise primarily from variations in charge, as opposed to broad compositional discrepancies. We used UV/vis absorption, fluorescence, and infrared spectroscopy to determine the optical and surface chemical properties of the charge-separated CDs, then incubated CDs with different surface charges in human cells. Using fluorescence microscopy, we measured their uptake and localization, which varied with surface charge and extent of amine passivation. Our data shows that charge plays an important role in the uptake of amine passivated CDs. To the best of our knowledge, this is the first study to explore differences in surface charge within a single, chemically similar group of CDs, and how these differences impact cellular uptake. By separating CDs solely based on their charge while maintaining their overall chemical composition, we are able to clearly demonstrate that even small charge variations within a population can influence how they are uptaken by cells.

Experimental and methods

Chemicals and reagents

Citric acid, diethylenetriamine (DT3), pentaethylenehexamine (PH6), acetone, ethanol and ammonium carbonate were purchased from Sigma Aldrich. Milli-Q water was produced in-house. Phosphate buffer solution (PBS, pH 7.4, 1×) and Dulbecco's Modified Eagle Medium (DMEM) were purchased from Wisent. HyCloneTM Cosmic Calf Serum (CCS) was purchased from Cytiva. WST-8 Cell Proliferation Assay Kit was purchased from Cayman Chemical. All reagents were of analytical grade and were used as is, without the need for further purification.

Synthesis of carbon dots

1.92 g (500 mM) of citric acid was added to 20 mL of water in a glass microwave reaction tube. 375 mM of the viscous amine precursor diethylenetriamine (DT3-CDs) or pentaethylenehexamine (PH6-CDs) was added and the solution was sonicated to ensure a homogeneous mixture. The mixture was placed into a CEM Discover SP microwave reactor at 210 °C for 10 minutes followed by another 10 minutes cooling period. After completion, the contents of the tubes were dialyzed in Milli-Q water using 3.5–5 kDa membranes for 5 days. After dialysis, the CD solution was concentrated and further purified

using organic washes of acetone and ethanol. After each wash the solution was mixed thoroughly using a vortex and then centrifuged at 10 000 rpm for 10 minutes. The pelleted, purified CDs were dried in an 80 °C oven and then crushed into a fine powder resulting in a reaction yield of approximately 10%.

Fluorescence spectroscopy analysis

A Cary Eclipse fluorescence spectrophotometer (Agilent Technologies) was utilized to acquire fluorescence spectra. The spectra were obtained by placing the sample in a 10 mm quartz cuvette and scanning the excitation wavelengths at intervals of 10 nm between 360 and 800 nm. The excitation and emission slits were adjusted to a width of 5 nm, and the PMT voltage was set at 600 V. The data was processed using Cary Eclipse software.

UV-vis absorbance spectroscopy

All absorbance spectra were acquired using a Cary 5000 series UV-vis-NIR spectrophotometer (Agilent Technologies). The UV-visible absorption spectra were collected over a range of 200–700 nm using a 1 cm quartz cuvette. A resolution of 1 nm and a bandwidth of 2 nm were set with a scan speed of 600 nm s^{-1}.

Fourier-Transform Infrared Spectroscopy (FT-IR) analysis

The Thermo Scientific Nicolet iS5, equipped with an ID5 attenuated total reflectance (ATR) accessory, was used to collect FT-IR data from dried CD samples. The analysis was performed on a laminate-diamond crystal window, with 64 scans taken at a resolution of 0.4 cm^{-1}. A gain of 1, an optical velocity of 0.4747 cm s^{-1}, and an aperture of 100 were consistently used for all measurements.

Transmission electron microscopy

TEM grids (3 mm, 200 mesh Lacey/carbon-coated copper grid) were prepared by pipetting a 2 μg mL^{-1} dispersion of each CD onto the grid followed by evaporation of the isopropanol solvent. TEM images were collected using a Talos microscope operating at 120 kV. The images were processed, and the carbon dot sizes were measured using Fiji imaging software. The TEM tiff files for each CD were opened in Fiji. Using the straight-line tool, the diameter (in nm) of a minimum of 50 to 100 individual nanoparticles was measured, and values were graphed in a histogram to reveal their Gaussian distribution.

X-ray photoelectron spectroscopy (XPS)

XPS spectra of the CDs were acquired using a Thermo Scientific K-alpha X-ray photoelectron spectrometer (ThermoFisher Scientific, Boston, MA, USA). Each analysis was carried out in triplicate, with 10 runs for each scan; the high-resolution and survey scans represent the average of the triplicate measurements.

Zeta potential

The zeta potential was measured with a Malvern Zetasizer Nano-S using a disposable folded capillary cell. The experiments were performed at 25 °C, and each sample was tested three times with 13–15 runs averaged for each test. The samples had a concentration of 0.5 mg mL^{-1} in Milli-Q water, and about 0.8 mL of the solution was used for the measurements. The software that comes with the infrastructure was utilized to analyze the data.

Ion exchange chromatography

40 mL of DEAE Sepharose fast flow anion exchange resin was poured into a glass column. The resin was washed and equilibrated with 30 mM ammonium carbonate buffer. 1.5 mL of a 0.05 g mL^{-1} water solubilized PH6-CD dispersion was added to the column and eluted using gradient elution ranging from 30 mM to 1 M ammonium carbonate. The column was washed with 1 M ammonium carbonate, and the resin was stored in a 20% ethanol solution. Once completed, the buffer was dried off and the zeta potential of the CDs was measured after resuspension in water.

log P partition coefficient for DT3-CDs and PH6-CDs

A series of standard solutions of the test compound in both water and octanol was prepared and their respective absorbance was measured. We then plotted the absorbance values against the corresponding concentrations to create calibration curves for water and octanol. The partition coefficient was determined by taking 5 mL of water and 5 mL of octanol and adding a known amount of DT3-CDs and or PH6-CDs. The solution was shaken vigorously for a sufficient time to allow equilibrium to be reached between the water and octanol phases, then the solution was given time to settle until the phases had visually separated. A sample of each phase was collected, and the absorbance was measured using the UV-visible spectrophotometer at the same wavelengths used for calibration.

The log P partition coefficient was then calculated using the following equation:

$$\log P = \log 10([\text{octanol}]/[\text{water}]) \tag{1}$$

where [octanol] and [water] are the concentrations of the compound in octanol and water, respectively.

Cell culture

HeLa cells were cultured in Dulbecco's modified Eagle medium (DMEM), supplemented with 10% (v/v) Cosmic Calf Serum (CCS; Wisent). Cells were incubated in a humidified environment set to 37 °C with 5% CO$_2$. Cell cultures were maintained by splitting them when they reached approximately 75–100% confluency or as needed for the experiments. To do this, cells were detached using trypsin and then diluted in fresh medium.

To investigate the uptake of CDs within HeLa cells, the cells were seeded on individual glass bottom dishes (CellVis) at a confluency of 30–40%. Cells were treated with 100 μL of each CD to reach a final concentration of 500 μg mL^{-1}. The cells were then left in an incubator for a period of 24 hours, after which their fluorescence intensity was measured *via* fluorescent microscopy. Prior to imaging, the cells were washed with 1×

PBS (phosphate-buffered saline) and replaced with fresh, pre-warmed media.

Cytotoxicity

HeLa cells were plated in 96-well dishes at 4000–5000 cells per well and left to adhere for 24 h. The cells were treated with increasing concentrations of each CD (0 to 10 000 µg mL^{-1}) for three generation times (72 h). Cytotoxicity was assessed using the WST-8 cell proliferation assay (Cayman Chemical) as per manufacturer's instructions. For each well, 10 µL of reagent was added for 4 hours, and the optical density (OD) values were obtained using the TECAN 200 PRO plate reader at a wavelength of 490 nm. Cell viability was measured as a ratio of the signal of treated cells vs. control (untreated cells):

$$\%\text{Cell viability} = \frac{\text{OD(490nm)}_{\text{sample}}}{\text{OD(490nm)}_{\text{control}}} \times 100\% \qquad (2)$$

The experiments were repeated in triplicate and the means and standard deviations were calculated and plotted using PRISM software. The IC$_{50}$ was obtained by measuring the concentration at which half the population (50%) remained alive after CD-treatment. HeLa cells were imaged using a Nikon brightfield microscope to ensure that they were plated with the appropriate confluency and to ensure that changes in density or metabolic activity were not caused by external contamination.

Microscopy

Cells were imaged using the Nikon-TiE inverted epifluorescence microscope with a Lambda XL Xenon light source and a 60× Plan Apo objective lens (NA 1.4) or a 100× S Fluor objective lens (NA 1.3), a Piezo Z stage (ASI), a Photometrics Evolve 512 EMCCD camera and Elements 4.0 acquisition software (Nikon). A Sutter Lambda XL Xenon-arc lamp filtered by a 380/12 nm bandpass filter was used to excite the CDs, and the emitted light was collected using a 400–600 nm bandpass filter (Chroma CT500/200bp). The images were exported as TIFFs and used for analysis.

Flow cytometry

HeLa cells were seeded 24 h before the uptake experiment, at 50 000 cells per well in 24-well plates. CDs were added to the cells at a final concentration of 500 µg mL^{-1}. Cells were incubated with the CDs for 24 h after incubation, cells were dissociated using trypsin, resuspended in PBS (Wisent) with 1 nM EDTA, 25 mM HEPESE pH 7.0 and 1% FBS, and then passed through a 40 µm strainer to remove large cell clumps. Cells were analysed using BD FACSVerse flow cytometer (BD Biosciences), 10 000 cells per sample. CDs detection: excitation wavelength at 405 nm and detection at 488/45 nm. Results were analysed with FlowJoV-10 program.

Statistical analysis

The TIFFs of HeLa cells treated with CDs were used to assess their uptake. The mean intensity was measured for each CD:

DT3-CDs (–): nHeLa = 41; DT3-CDs (+): nHeLa = 32; PH6-CDs (–): nHeLa = 32; and PH6-CDs (+): nHeLa = 27. The mean intensity values of the whole cell region were then plotted on a whisker box plot and a one-way ANOVA was performed along with a *post hoc* paired *t*-test to assess for statistical significance.

Lastly, the TIFFs were also used to measure the proportion of CDs in the cytosol of HeLa cells. The images were background-corrected, and the mean intensity was determined from the average of three regions of interest in the cytosol for the different CDs: DT3-CDs (–): nHeLa = 50; DT3-CDs (+): nHeLa = 53; PH6-CDs (–): nHeLa = 36; and PH6-CDs (+): nHeLa = 27. The mean intensity values were plotted on a whisker box plot and a one-way ANOVA was performed along with a *post hoc* paired *t*-test to determine statistical significance.

Results and discussion

Optical properties of CDs

To assess the optical properties and how they relate to structural features UV-vis and fluorescence spectroscopy was carried out. First, amine passivated CDs were synthesized using a microwave assisted route with citric acid as the carbon-source and diethylenetriamine (DT3), or pentaethylenehexamine (PH6) as passivating agents. Following synthesis, the optical, physical and chemical properties of the CDs were assessed. The CDs were first characterized using absorption and fluorescence spectroscopy. The UV-vis profile of the DT3-CDs and PH6-CDs are presented in Fig. 1A and B, respectively. Notably, two main absorption bands at 240 and 355 nm show the characteristic $\pi \rightarrow \pi^*$ and $n \rightarrow \pi^*$ electronic transitions of amine-passivated dots. The $\pi \rightarrow \pi^*$ transition at 240 nm can be attributed to the conjugated core, while the $n \rightarrow \pi^*$ transition is characteristic of the double bonded heteroatoms decorating the surface of the CDs. These are typically C=O and C=N groups originating from amide, carboxylic acid and nitrogen containing groups on the surface.[65] The fluorescence emission profiles contain distinct emission maxima at 440 and 445 nm, respectively, when excited by 350 nm light. It is hypothesized that this emission signature originates from the surface domains unique to these amine-passivated CDs.[57]

Physico-chemical properties of CDs

The size and shape of the CDs were characterized by TEM, as depicted in Fig. 1C. The CDs were 3.3 nm in size with a distribution spanning from 0.5 to 6 nm and had a quasi-spherical morphology. It should be noted that obtaining high-resolution TEM images of CDs remains a technical challenge primarily due to a lack of atoms with high atomic numbers resulting in weak electron scattering and inherently low image contrast. Additionally, their amorphous nature results in the lack of electron diffraction patterns further contributing to the challenge. Despite the limitations, the TEM images provided are consistent with those frequently reported for CDs in the literature.[66] Fourier-Transform Infrared Spectroscopy (FT-IR) was then used to evaluate the surface functional groups of the CDs. Fig. 1D shows the FT-IR spectra of DT3-CDs and PH6-CDs
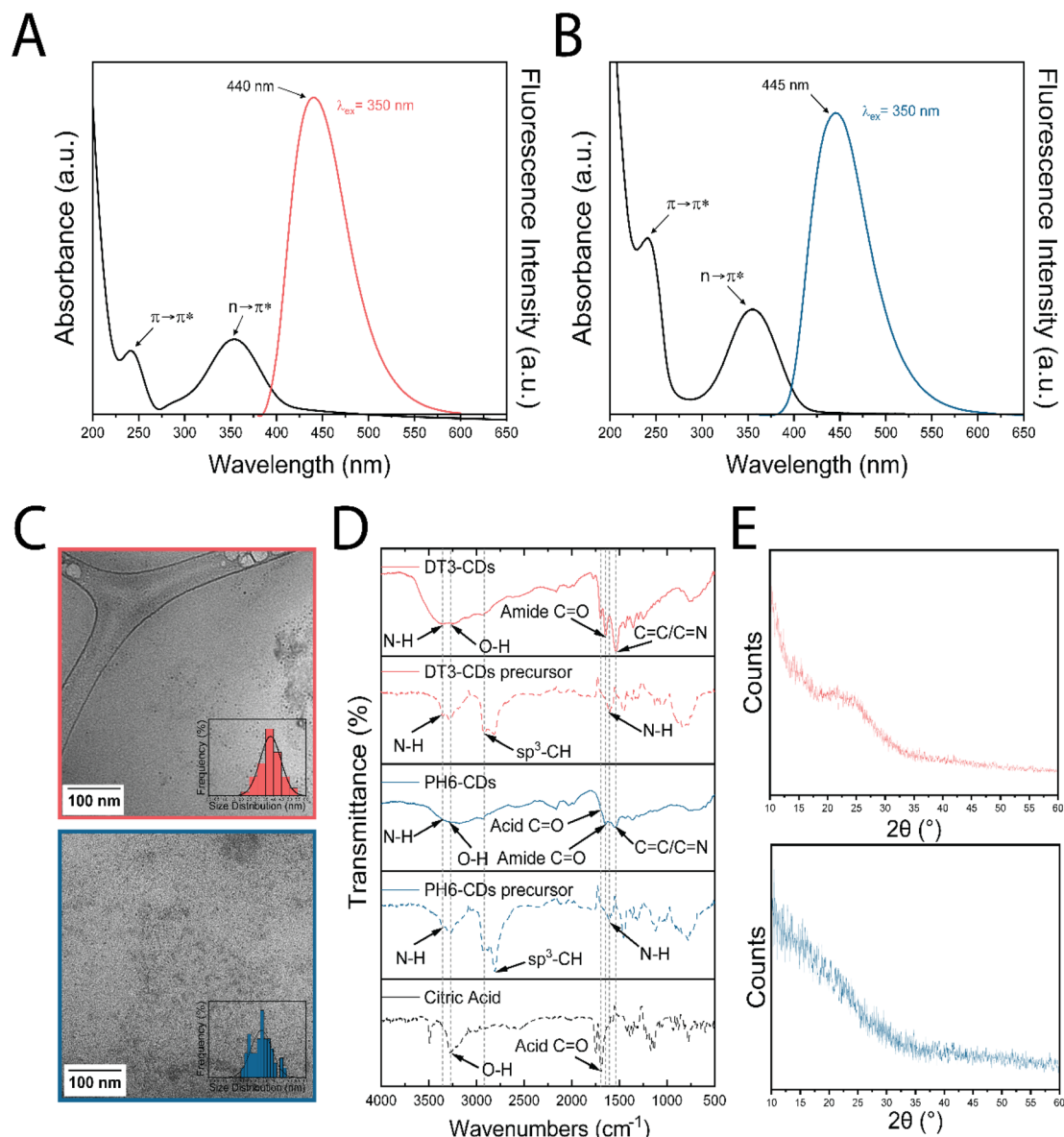
Fig. 1 Optical and physico-chemical properties of DT3-CDs and PH6-CDs. (A) and (B) Room temperature absorbance and fluorescence spectra of each CDs in an aqueous solution. The UV-vis absorption spectrum the CDs (black curve) reveals two absorption bands centered at 240 nm and 335–355 nm, which reflect the $\pi \rightarrow \pi^*$ and $n \rightarrow \pi^*$ transition, respectively. Following maximum excitation at 350 nm one emission maxima is measured at 440 nm for DT3-CDs and 445 nm for PH6-CDs (colored curve). (C) CDs are quasi-spherical and average 3.54 nm in size. TEM images show aqueous dispersions with sizes of 3.8 ± 0.7 nm for DT3-CDs (top panel) and 3.3 ± 0.4 nm for PH6-CDs (lower panel). The size measurements for each of the CDs were spread over a Gaussian distribution ranging from 0 to 6 nm (D) FT-IR spectra for each CD along with their respective precursors (dotted line). The broad O–H stretch at 3250 cm^{-1} indicates a carboxylic acid functionality, and sp^3 and sp^2 C–H stretches can be seen at 2964 cm^{-1} and 2830 cm^{-1} respectively. Lastly, amide C=O, C=C/C=N, and N–H/C–N peaks appears at 1646 cm^{-1}, 1536 cm^{-1} and 1354 cm^{-1}. (E) XRD profile for DT3-CDs (top panel) and PH6-CDs (lower panel) CDs showing an amorphous halo in the range of 10–60° 2θ.

were compared with their respective precursors. The spectrum of citric acid includes an O–H stretching signal at 3250 cm^{-1}, attributed to the carboxylic acid (–COOH), and corresponding carbonyl stretches at 1715 cm^{-1}. Diethylenetriamine and pentaethylenehexamine caused distinct signals at 3260 cm^{-1} ascribed to primary aliphatic amines accompanied by sp^3 C–H stretches at 2964 cm^{-1} and sp^2 C–H stretches at 2830 cm^{-1}. In addition, a signal at 1580 cm^{-1} was likely caused by N–H bending, which is characteristic of amines. Comparing the

precursor spectra with the CDs revealed marked distinctions. Both DT3-CD and PH6-CD spectra included carboxylic acid stretches ranging from 3450 to 2600 cm^{-1} (COOH) along with carbonyl stretches at 1715 cm^{-1}. Notably, a distinctive C=O stretch, characteristic of amides, emerged at 1645 cm^{-1}, while C=C/C=N stretches at 1550 cm^{-1} were consistent with variable functional groups. All stretches and bends are in accordance with other similar CDs discussed in the literature.[1,57,67] The similarities in spectra between the precursors and CDs supports

that the amine-passivated CDs were successfully synthesized. Disparities between DT3-CDs and PH6-CDs were observed in their distinct carboxyl/amide/amine stretches. Notably, for the PH6-CDs, the decrease in carboxyl bands compared to amines is consistent with an increase in amine passivation.

To further validate the FT-IR findings and confirm the presence of surface functional groups, X-ray photoelectron spectroscopy (XPS) was used. The binding energies for C1s, N1s, and O1s were measured at 280, 400, and 530 eV, respectively, and reveal the elemental composition of DT3-CDs and PH6-CDs (Fig. S1). Both CDs exhibited similar carbon content with values of 65.50% and 69.66%, respectively. However, they had distinct oxygen and nitrogen content. DT3-CDs contained 14.50% nitrogen and 19.59% oxygen, whereas PH6-CDs exhibited 16.93% nitrogen and 13.29% oxygen. The decrease in oxygen content in PH6-CDs aligns with the reduction in carboxyl/amide peaks observed in the FT-IR analysis. Further analysis revealed specific chemical bonding and composition. For DT3-CDs, the C1s peaks at 285, 286, and 288 eV correspond to C–C, C–N, and carboxyl C=O groups, respectively. The N1s peak peaks at 399, 400, and 401 eV can be attributed to pyridinic, pyrrolic and graphitic nitrogen, respectively. Meanwhile, for PH6-CDs, C1s peaks at 285, 286, and 287 eV correspond to C–C, C–N, and carboxyl C=O bonds, while the N1s peaks at 398, 399, and 400 eV represent amines, amides, and protonated amines, represent pyridinic, pyrrolic and graphitic nitrogen, respectively. For both CDs, the O1s peaks at 531 and 532 eV indicate carboxyl C=O and carbonyl C–O groups. All binding energy assignments are in good accordance with current CD literature.[57,68] X-ray Diffraction (XRD) was then carried out to determine the crystallinity of the CDs. The absence of a crystalline structure was observed, as shown in Fig. 1E. The XRD profile also showed a distinct amorphous halo spanning the 10–30° range, which corresponds to the graphitic core of the CDs.

Charge separation using column chromatography

In order to study surface charge, zeta potential measurements were carried out. The mean zeta potential for the unseparated parent DT3-CDs was measured to be −32 mV, while that of the unseparated parent PH6-CDs was +4 mV. This difference in zeta potential reflects the extent of amine passivation. PH6-CDs likely consist of more primary amines, whereas DT3-CDs are composed of more electronegative carboxylic groups. DT3-CDs and PH6-CDs were separated into distinct subgroups based on charge using ion exchange column chromatography, a well-established method that has been used previously for separation of compounds based on differences in their net charges.[69] An overview of this method can be observed in Fig. 2A. As demonstrated in Fig. 2B, DT3-CDs were separated into five distinct fractions of −14, −16, −24, −27 and −35 mV, while PH6-CDs were separated into +7, 0, −1, −3, and 6 mV. The fractions for each CD were further characterized using UV-vis spectroscopy as shown in Fig. S2A, and all had absorption peaks at 240 nm and 350 nm, suggesting they have similar optical profiles. Their fluorescence emission spectra were also similar as shown in Fig. S2B. FT-IR was also used to determine potential differences

in the chemical composition of the charge separated CDs (Fig. 2C and S3). There was discernible augmentation in the C=O amide stretch (red band) compared to the C=C/C=N stretch (yellow band) for the most positively and negatively charged CDs. We hypothesize that the protonation of these groups is primarily responsible for dictating surface charge and thus ion-exchange yields CDs differing in C=O and C=C/C=N groups. Additionally, the ratio of amines to amides decreased with an increase in negative charge due to the acidic nature of the amide groups (green band). The availability of the lone pair of electrons on the amide nitrogen atom for donation was attenuated, leading to reduced protonation (positive charge), and instead is involved in resonance with the associated carbonyl group, augmenting the negative surface charge.[70] Lastly, as shown in Fig. S3, there was an increase in the resolution of the FT-IR peaks compared to the parent CDs, which would be expected with isolated populations of CDs with identical (vs. similar) chemical composition.

Cytotoxicity of CDs in HeLa cells

In order to study the cytotoxicity of the charge-separated CDs in HeLa cells a WST-8 cell viability assay was carried out. Fractions 1 and 5 showed the highest net difference in charge (−14 vs. −35 mV for DT3-CDs, and +7 vs. −6 mV for PH6-CDs), and were used to reveal how surface charge impacts cell viability. Hereafter, these fractions are referred to as DT3-CDs (+) and DT3-CDs (−), and PH6-CDs (+) and PH6-CDs (−), respectively. After exposing HeLa cells to varying concentrations of the CDs for three division cycles (72 hours). As shown in Fig. S4, all of the charge-separated amine-passivated CDs caused negligible or low cytotoxicity. Among the discernible IC$_{50}$ values, PH6-CDs (+) had a value of 4200 µg mL^{-1}, followed by PH6-CDs (−) at 7500 µg mL^{-1}, and DT3-CDs (+) at 8500 µg mL^{-1}. Notably, DT3-CDs (−) exhibited no toxicity even beyond a concentration of 10 000 µg mL^{-1}. Since none of the CDs caused significant toxicity, we tested their uptake and localization in cells.

Cellular uptake of CDs separated by charge

To determine how surface charge affects cellular uptake, HeLa cells were treated with DT3-CDs (−), DT3-CDs (+), PH6-CDs (−) and PH6-CDs (+), and cells were imaged by fluorescence microscopy after 24 hours where increase in fluorescence intensity correlates to greater cellular uptake. As shown in Fig. 3A cells exposed to DT3-CDs (+) demonstrated a significant 1.17 fold increase in mean fluorescence compared to DT3-CDs (−) (Fig. 3B and Table S1). In addition, DT3-CDs (+) were 4.12-fold enriched in the cytosol compared to DT3-CDs (−) (Fig. 3C and Table S1). Although FT-IR analysis revealed no differences in functional groups between DT3-CDs (+) and DT3-CDs (−), their difference in surface charge could be due to aliphatic hydrocarbons, which would confer a change in amphiphilicity. To test this theory, a log$P$ analysis on the −35 mV fraction of DT3-CDs revealed a log$P$ value of −0.95, suggesting they are mostly found in the aqueous layer. However, the −14 mV DT3-CDs had a log$P$ of −0.18, and this near neutral value suggests that these CDs are almost equally partitioned between the lipid and aqueous phases. Notably, the log$P$ value of the PH6-CD (−)
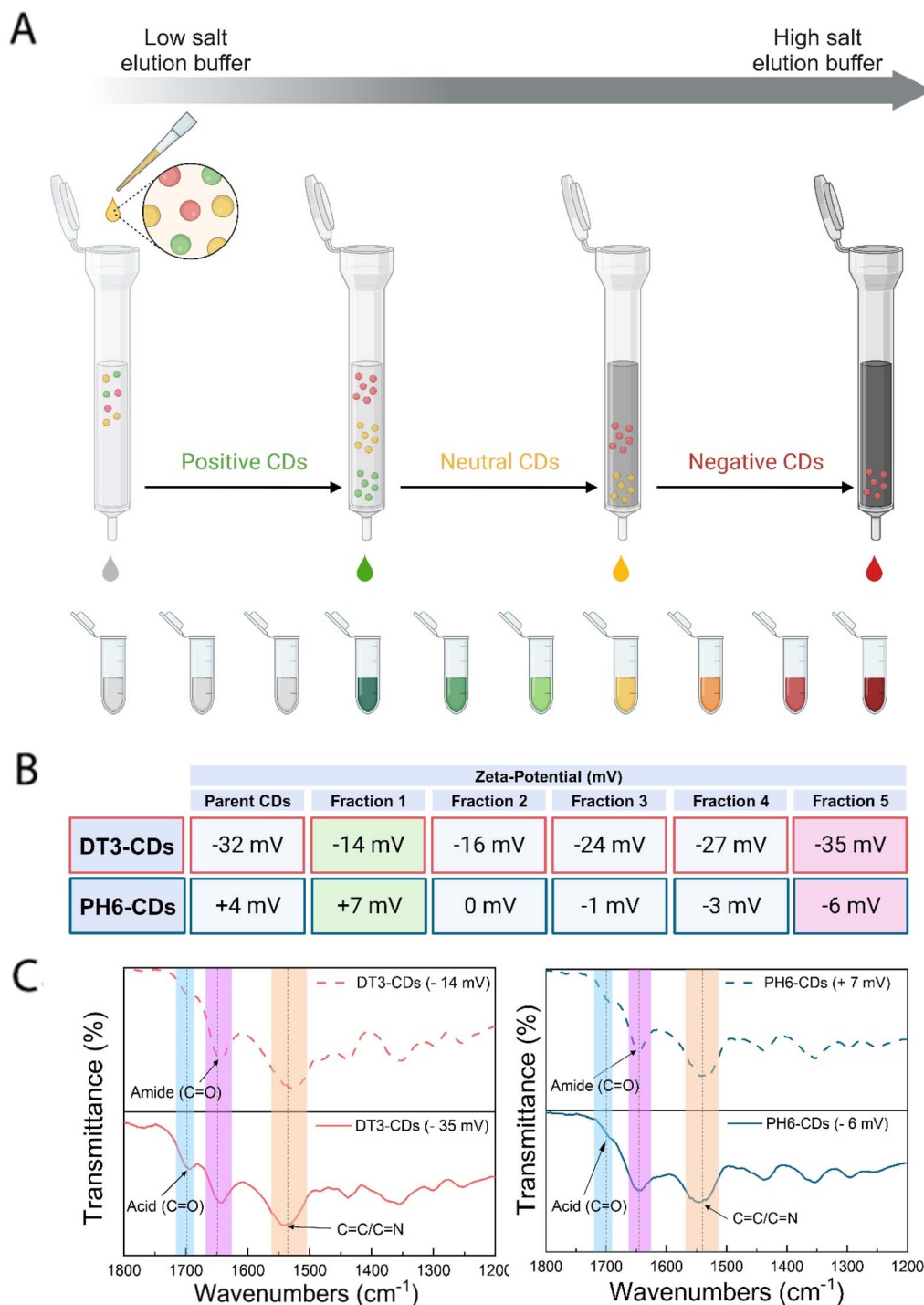
Fig. 2 Charge separation using ion chromatography. (A) Schematic representation of the ion chromatography process. As higher salt elution buffer is added to the resin column, more negatively charged CDs are eluted out of the column and collected. Lower salt elution buffer allows to collect and separate from the parent CDs more positively charged CDs. (B) Table showing the individual zeta potential measurements before and after the separation of each of the parent CDs. Highlighted in green are the least negatively charged CDs and in pink are the most negatively charged ones. (C) FT-IR spectra of the most negative and least negative fraction for each CDs. An increase in amine functionalities is observable with a decrease in negative charge.

parent was −0.85, which is very similar to DT3-CDs (−) indicating comparable amphiphilicity. This aligns with their similar subcellular localization patterns observed in Fig. 3C and 4A. The small size and amphiphilic property of DT3-CDs (+)

suggests that they could enter cells passively highlighting potential applications in drug delivery. This is in concordance with our previously published research and aligns with findings from other authors.[1,71]
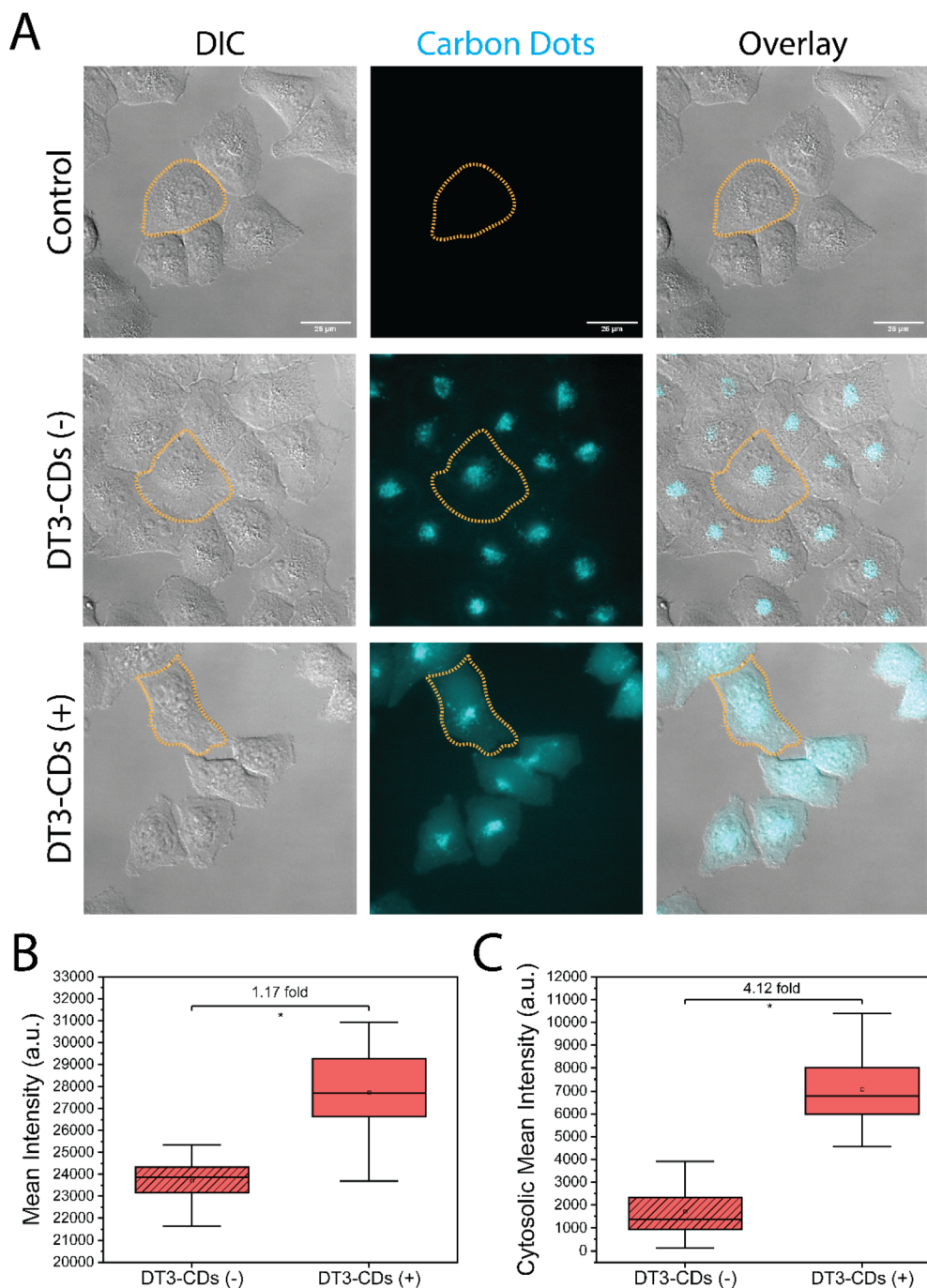
Fig. 3 Cellular uptake of DT3-CDs in HeLa cells. (A) Brightfield (left), fluorescence images (middle), and an overlay (right) of HeLa Cells 24 hours after treatment with the DT3-CDs (−) and DT3-CDs (+) (blue signal). The scale bar is 25 μm. (B) A box and whiskers plot show the cytosolic mean intensity (a.u.) for the DT3-CDs (−) and the DT3-CDs (+). Bars indicate standard deviation. One-way ANOVA and paired t-tests to DT3-CDs were done to show significance (*$p < 0.05$). (C) A box and whiskers plot show the mean intensity (a.u.) of the DT3-CDs (−) and the DT3-CDs (+). Bars indicate standard deviation. One-way ANOVA and paired t-tests to DT3-CDs were done to show significance (*$p < 0.05$).

Next, we determined how different PH6-CDs, which have more positive surface charges compared to the DT3-CDs, interact with cells. HeLa cells were treated for 24 hours with PH6-CDs (−) and PH6-CDs (+) and imaged fluorescence microscopy (Fig. 4A). A rather minor, yet significant 1.04-fold increase in the mean fluorescence intensity for PH6-CDs (+) compared to PH6-CDs (−) was noted (Fig. 4B and Table S2). In

addition, neither CD localized to the cytosol (Fig. 4C and Table S2). Since PH6-CDs were passivated with a precursor containing more amines compared to DT3, this could cause the PH6-CDs to have increased hydrophilicity and fewer aliphatic entities, requiring them to rely on endocytosis for cellular uptake. In support of this, both (+) and (−) PH6-CDs appeared to be strongly enriched in the perinuclear region of the cell, as well as
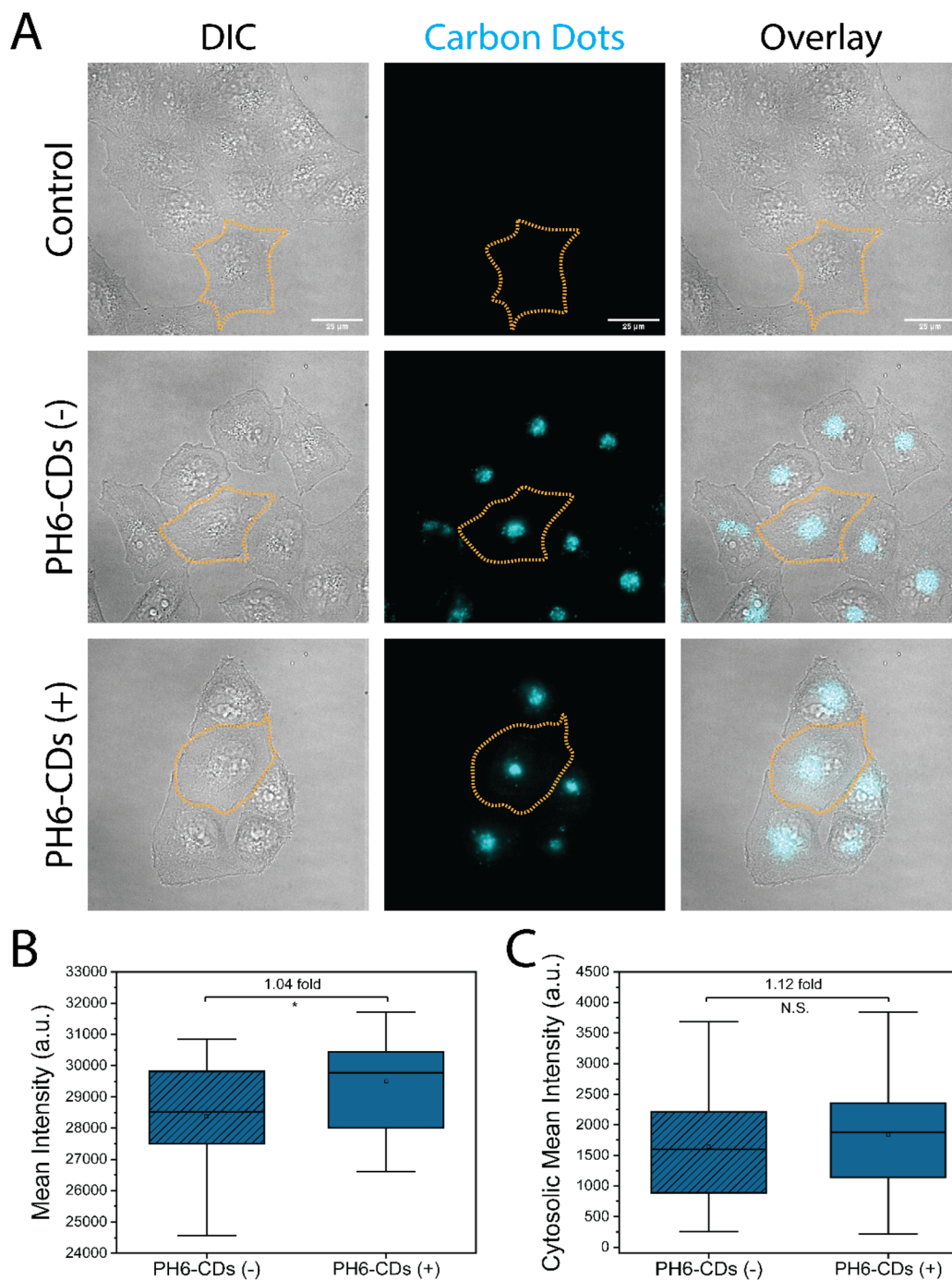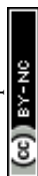
Fig. 4 Cellular uptake of PH6-CDs in HeLa cells. (A) Brightfield (left), fluorescence images (middle), and an overlay (right) of HeLa Cells 24 hours after treatment with the PH6-CDs (−) and PH6-CDs (+) (blue signal). The scale bar is 25 μm. (B) A box and whiskers plot show the cytosolic mean intensity (a.u.) for the PH6-CDs (−) and the PH6-CDs (+). Bars indicate standard deviation. One-way ANOVA and paired t-tests to PH6-CDs were done to show significance (*$p < 0.05$). (C) A box and whiskers plot show the mean intensity (a.u.) of the PH6-CDs (−) and the PH6-CDs (+). Bars indicate standard deviation. One-way ANOVA and paired t-tests to PH6-CDs were done to show significance (*$p < 0.05$).

in the lysosomes as previously reported for PH6-CDs and other similar CDs.[1,72–74]

A summary of our findings is shown in Fig. 5A, where a schematic shows how the fluorescence intensity of CDs in cells increases with their surface charge. Our findings are in agreement with the literature, where prior studies revealed that positively charged nanoparticles enter cells more easily compared to negatively charged counterparts.[63] This is likely because the positively charged particles can more strongly interact with the negatively charged phospholipids in the plasma membrane, which could cause them to accumulate nearby for endocytic uptake.[75] This is shown in Fig. 5B where
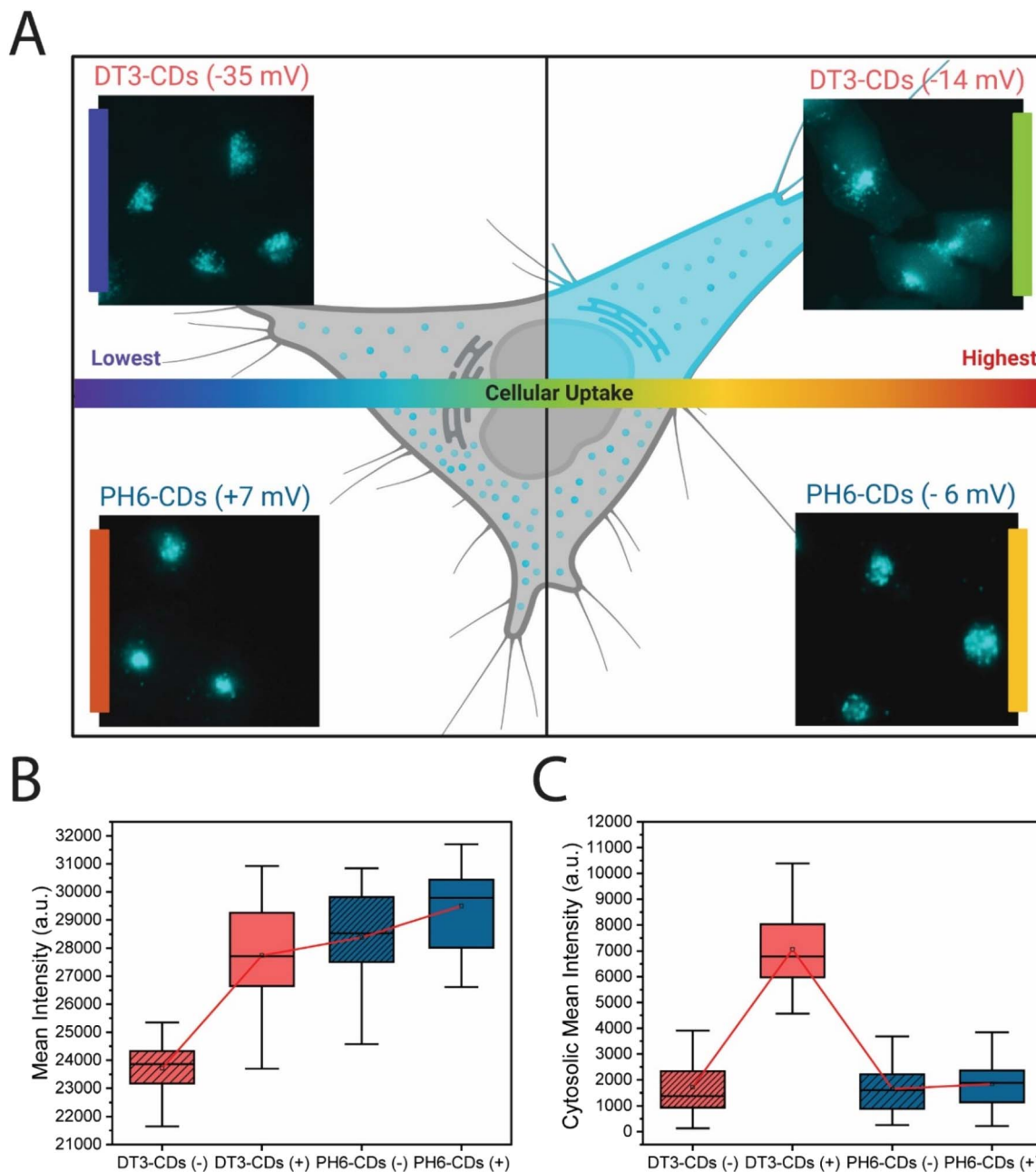
Fig. 5   Cellular uptake comparison of DT3-CDs and PH6-CDs in HeLa cells. (A) Schematic representation of the localization and cellular uptake of CDs in HeLa cells. More positive CDs shows more cellular uptake (PH6-CDs) *vs.* more negatively charged CDs (PH6-CDs). DT3-CDs (+) can enter cells passively and localize to the cytosol. (B) A box and whiskers plot shows the mean intensity (a.u.) of each CDs going from the most negative to the most positive (−35 mV, −14 mV, −6 mV and +7 mV). Bars indicate standard deviation. The red line shows a positive correlation. (C) A box and whiskers plot shows the cytosolic mean intensity (a.u.) of each CD going from the most negative to the most positive. Bars indicate standard deviation. The red line links each mean.

the different intensities are compared for DT3 and PH6-CDs on the same graph, demonstrating a positive correlation where each incremental change in surface charge corresponds to an increase in fluorescence intensity, thus an increase in cellular uptake. Fig. 5C also shows that amphiphilic CDs can enter cells passively based on the increased cytosolic localization of DT3-CDs (+) compared to their hydrophilic counterparts, or the hydrophilic PH6-CDs. Additionally, while DT3-CDs (−) have more intense COOH stretching compared to DT3-CDs (+), as depicted in the FT-IR in Fig. 2C, their amine and amide bands are similar. Therefore, the observed differences in uptake and localization can likely be attributed to their respective sp^2 conjugation. This is supported by the FTIR data, which showed that DT3-CDs (+) appear to be composed of more sp^2 hybridized carbons relative to DT3-CDs (−). These differences likely occur during their synthesis.

Lastly, flow cytometry was performed as an optical assay to confirm our findings and determine how surface charge affects cellular uptake as shown in Fig. 5. The same protocol was used for flow cytometry to ensure consistency in the experimental conditions. DT3-CDs (+), DT3-CDs (−), PH6-CDs (+), and PH6-CDs (−) samples were excited at 405 nm and fluorescence emission at 450 nm was captured. As shown in Fig. S5, 96–100% of the cells were fluorescent meaning that all cells within the population internalized the carbon dots. Since the incubation time is equivalent to the doubling time of the cells, this suggest that we reached saturation. According to Fig. S5, the fluorescence intensity increases with the surface charge. Flow cytometry analysis revealed a comparable positive trend between the mean fluorescence intensity of samples and fluorescence microscopy analysis (Fig. 5).

It is important to note that, although flow cytometry is a popular method for quantifying cellular uptake of nanoparticles, live imaging fluorescent microscopy is necessary to complete the analysis. Fluorescent microscopy, when performed properly, can have a strong impact both quantitatively and qualitatively for measuring cellular uptake. While flow cytometry allows analysis of cellular populations, it lacks the spatial information provided by fluorescent microscopy. However, it does not discriminate between different cellular compartments and has lower sensitivity for detecting subtle changes in nanoparticle composition, as seen in our results. Specifically, when discussing spatial resolution and discerning between subcellular localization, we refer to cytosolic *versus* perinuclear/nuclear regions. The nuclear region, being deeper within the cell, can be more challenging to detect using flow cytometry, whereas cytosolic or surface signals are more easily picked up. These differences can be effectively captured using fluorescence microscopy. Therefore, integrating fluorescent microscopy with flow cytometry can provide a comprehensive understanding of nanoparticle uptake, combining the strengths of both techniques and thus confirming findings. It should be noted that quantum yield is not the primary determinant of fluorescence in cells, as PH6-CDs with a lower yield (20%) exhibited brighter intracellular fluorescence than DT3-CDs with a higher yield (26%). It should also be noted that quantum yield should not be considered a primary factor when evaluating fluorescence in cellular contexts as the quantum yield of unseparated parent PH6-CDs with a lower quantum yield of 20% exhibited brighter intracellular fluorescence in comparison to unseparated parent DT3-CDs with a higher quantum yield of 26%. This suggests that fluorescence observed in cells is driven more by differences in cellular uptake and subcellular localization than by quantum yield alone.

Conclusions

Our work aimed to shed light on the relationship between surface charge and chemical composition of carbon dots and how this impacts their cellular uptake and localization in HeLa cells. By systematically investigating CDs with varying surface charges and chemical properties, we have unravelled novel insights that bridge the gap in our understanding of how CDs

interact with cells. While previous studies suggested that surface charge can impact cellular uptake, we obtained direct evidence for this by comparing different sets of CDs with the same composition. Our findings show that as the surface charge of CDs increases, there is an increase in their cellular uptake. With the most notable cellular uptake increase being for charge separated DT3 CDs by 1.17-fold and a 4.12-fold increase in cytosolic localization. However, we also demonstrate that amphiphilicity, likely caused by an increase in aliphatic hydrocarbons, facilitates passive entry. These CDs could be exploited for the efficient delivery of drugs where the mechanism of action is in the cytosol, providing a unique drug delivery strategy. The absence of any cytosolic fluorescence signal from PH6-CDs regardless of surface charge emphasizes the intricate interplay between surface charge and chemical composition when considering how CDs interact with cells. Given that these CDs likely enter cells *via* endocytosis and accumulate in the lysosomes, this property could render them useful for different applications. Collectively, our findings provide valuable insights into the design and optimization of CDs for enhanced cellular delivery, and for applications in drug delivery, or as bioimaging tools.

Author contributions

Conceptualization, Adryanne Clermont-Paquette, Gianluca Fuoco and Rafik Naccache; funding acquisition, Alisa Piekny and Rafik Naccache; methodology, Adryanne Clermont-Paquette, Gianluca Fuoco, Cecilia R. Brancheriau, Alisa Piekny and Rafik Naccache; resources, Alisa Piekny and Rafik Naccache; writing – original draft, Adryanne Clermont-Paquette, Gianluca Fuoco, Alisa Piekny and Rafik Naccache; writing – review & editing, Adryanne Clermont-Paquette, Gianluca Fuoco, Cecilia R. Brancheriau, Alisa Piekny and Rafik Naccache.

Conflicts of interest

There are no conflicts to declare.

Data availability

The authors confirm that the data supporting the findings of this study are available within the article. Additionally, the data supporting this article have been included as part of the SI.

Supplementary characterization of parent and charge seperated fractions including cell viability and cellular uptake studies. See DOI: **https://doi.org/10.1039/d5ra03738g**.

Acknowledgements

University with the help of Nooshin Movahed. XPS studies were performed at McGill University (MIAM Facilities in the Department of Mining and Materials Engineering) with the assistance of Lihong Shang. Microscopy was performed in the Centre for Microscopy and Cellular Imaging at Concordia University with the help of Dr Chris Law. Parts of some figures were created with BioRender.com.

Notes and references

1 A. Clermont-Paquette, K. Larocque, A. Piekny and R. Naccache, *Mater. Adv.*, 2024, **5**, 3662–3674.

2 H. Wang, P. Sun, S. Cong, J. Wu, L. Gao, Y. Wang, X. Dai, Q. Yi and G. Zou, *Nanoscale Res. Lett.*, 2016, **11**, 27.

3 C. Hu, M. Li, J. Qiu and Y. P. Sun, *Chem. Soc. Rev.*, 2019, 2315–2337, DOI: 10.1039/c8cs00750k.

4 J. J. Huang, Z. F. Zhong, M. Z. Rong, X. Zhou, X. D. Chen and M. Q. Zhang, *Carbon N. Y.*, 2014, **70**, 190–198.

5 S. Cailotto, R. Mazzaro, F. Enrichi, A. Vomiero, M. Selva, E. Cattaruzza, D. Cristofori, E. Amadio and A. Perosa, *ACS Appl. Mater. Interfaces*, 2018, **10**, 40560–40567.

6 A. Macina, T. V. De Medeiros and R. Naccache, *J. Mater. Chem. A*, 2019, **7**, 23794–23802.

7 G. Filippini, M. Prato and C. Rosso, *Am. Chem. Soc.*, 2020, 8090–8105, DOI: 10.1021/acscatal.0c01989.

8 S. D. Hettiarachchi, R. M. Graham, K. J. Mintz, Y. Zhou, S. Vanni, Z. Peng and R. M. Leblanc, *Nanoscale*, 2019, **11**, 6192–6205.

9 H. Li, X. Yan, D. Kong, R. Jin, C. Sun, D. Du, Y. Lin and G. Lu, *Nanoscale Horiz.*, 2020, **5**, 218–234.

10 Q. Zeng, D. Shao, X. He, Z. Ren, W. Ji, C. Shan, S. Qu, J. Li, L. Chen and Q. Li, *J. Mater. Chem. B*, 2016, **4**, 5119–5126.

11 L. Li, C. Lu, S. Li, S. Liu, L. Wang, W. Cai, W. Xu, X. Yang, Y. Liu and R. Zhang, *J. Mater. Chem. B*, 2017, **5**, 1935–1942.

12 P. Shen, J. Gao, J. Cong, Z. Liu, C. Li and J. Yao, *ChemistrySelect*, 2016, **1**, 1314–1317.

13 Q. Wang, X. Huang, Y. Long, X. Wang, H. Zhang, R. Zhu, L. Liang, P. Teng and H. Zheng, *Carbon N. Y.*, 2013, **59**, 192–199.

14 P. Das, S. Ganguly, P. K. Marvi, M. Sherazee, X. (Shirley) Tang, S. Srinivasan and A. R. Rajabzadeh, *Adv. Mater.*, 2024, **36**, 2409819.

15 S. Khan, N. C. Verma, C. Rao and C. K. Nandi, *ACS Appl. Nano Mater.*, 2018, **1**, 483–487.

16 T. V de Medeiros, J. Manioudakis, F. Noun, J.-R. Macairan, F. Victoria and R. Naccache, *J. Mater. Chem. C*, 2019, **7**, 7175–7195.

17 F. Yan, Z. Sun, H. Zhang, X. Sun, Y. Jiang and Z. Bai, *Microchim. Acta*, 2019, **186**, 1–37.

18 A. B. Siddique, A. K. Pramanick, S. Chatterjee and M. Ray, *Sci. Rep.*, 2018, **8**, 9770.

19 M. K. Barman and A. Patra, *J. Photochem. Photobiol. C*, 2018, **37**, 1–22, DOI: 10.1016/j.jphotochemrev.2018.08.001.

20 K. Hola, A. B. Bourlinos, O. Kozak, K. Berka, K. M. Siskova, M. Havrdova, J. Tucek, K. Safarova, M. Otyepka, E. P. Giannelis and R. Zboril, *Carbon N. Y.*, 2014, **70**, 279–286.

21 W. Liu, C. Li, Y. Ren, X. Sun, W. Pan, Y. Li, J. Wang and W. Wang, *J. Mater. Chem. B*, 2016, 5772–5788, DOI: 10.1039/c6tb00976j.

22 S. Sahu, B. Behera, T. K. Maiti and S. Mohapatra, *Chem. Commun.*, 2012, **48**, 8835–8837.

23 Z. Li, Y. Zhang, Q. Niu, M. Mou, Y. Wu, X. Liu, Z. Yan and S. Liao, *J. Lumin.*, 2017, **187**, 274–280.

24 W. Li, Z. Yue, C. Wang, W. Zhang and G. Liu, *RSC Adv.*, 2013, **3**, 20662–20665.

25 J. Jia, B. Lin, Y. Gao, Y. Jiao, L. Li, C. Dong and S. Shuang, *Spectrochim. Acta, Part A*, 2019, **211**, 363–372.

26 J. Schneider, C. J. Reckmeier, Y. Xiong, M. Von Seckendorff, A. S. Susha, P. Kasak and A. L. Rogach, *J. Phys. Chem. C*, 2017, **121**, 2014–2022.

27 Y. Jiang, Q. Han, C. Jin, J. Zhang and B. Wang, *Mater. Lett.*, 2015, **141**, 366–368.

28 K. J. Mintz, G. Mercado, Y. Zhou, Y. Ji, S. D. Hettiarachchi, P. Y. Liyanage, R. R. Pandey, C. C. Chusuei, J. Dallman and R. M. Leblanc, *Colloids Surf., B*, 2019, **176**, 488–493.

29 F. Li, Y. Li, X. Yang, X. Han, Y. Jiao, T. Wei, D. Yang, H. Xu and G. Nie, *Angew. Chem., Int. Ed.*, 2018, **57**, 2377–2382.

30 M. Zhang, L. Hu, H. Wang, Y. Song, Y. Liu, H. Li, M. Shao, H. Huang and Z. Kang, *Nanoscale*, 2018, **10**, 12734–12742.

31 S. Ahmadian-Fard-Fini, D. Ghanbari and M. Salavati-Niasari, *Composites, Part B*, 2019, **161**, 564–577.

32 Y. N. Monday, J. Abdullah, N. A. Yusof, S. A. Rashid and R. H. Shueb, *Appl. Sci.*, 2021, **11**, 1–17.

33 W. Zhang, X. Fang, F. He, J. Bai, Y. Cheng, K. Weerasinghe, X. Meng, H. Xu and T. Ding, *J. Phys. Chem. C*, 2021, **125**, 5207–5216.

34 X. Wang, K. Qu, B. Xu, J. Ren and X. Qu, *J. Mater. Chem.*, 2011, **21**, 2445–2450.

35 T. N. J. I. Edison, R. Atchudan, M. G. Sethuraman, J. J. Shim and Y. R. Lee, *J. Photochem. Photobiol. B*, 2016, **161**, 154–161.

36 D. M. A. Crista, J. C. G. E. da Silva and L. P. da Silva, *Nanomaterials*, 2020, **10**, 1–15.

37 S. Zhang, L. Zhang, L. Huang, G. Zheng, P. Zhang, Y. Jin, Z. Jiao and X. Sun, *J. Lumin.*, 2019, **206**, 608–612.

38 L. Li and T. Dong, *J. Mater. Chem. C*, 2018, **6**, 7944–7970.

39 C. Liu, P. Zhang, X. Zhai, F. Tian, W. Li, J. Yang, Y. Liu, H. Wang, W. Wang and W. Liu, *Biomaterials*, 2012, **33**, 3604–3613.

40 S. Liang, M. Wang, W. Gao and X. Zhao, *Opt. Mater.*, 2022, **128**, 112471.

41 A. Kundu, J. Lee, B. Park, C. Ray, K. V. Sankar, W. S. Kim, S. H. Lee, I. J. Cho and S. C. Jun, *J. Colloid Interface Sci.*, 2018, **513**, 505–514.

42 C. Wang, Z. Xu and C. Zhang, *ChemNanoMat*, 2015, **1**, 122–127.

43 K. Radhakrishnan and P. Panneerselvam, *RSC Adv.*, 2018, **8**, 30455–30467.

44 S. Y. Lim, W. Shen and Z. Gao, *Chem. Soc. Rev.*, 2015, 362–381, DOI: 10.1039/c4cs00269e.

45 A. P. Demchenko and A. P. Demchenko, *Introduction to Fluorescence Sensing: Volume 1: Materials and Devices*, 2020, pp. 357–399.
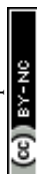
46 S. Khan, A. Gupta, N. C. Verma and C. K. Nandi, *Nano Lett.*, 2015, **15**, 8300–8305.

47 S. Khan, W. Li, N. Karedla, J. Thiart, I. Gregor, A. M. Chizhik, J. Enderlein, C. K. Nandi and A. I. Chizhik, *J. Phys. Chem. Lett.*, 2017, **8**, 5751–5757.

48 K. Hola, Y. Zhang, Y. Wang, E. P. Giannelis, R. Zboril and A. L. Rogach, *Nano Today*, 2014, **9**(5), 590–603, DOI: **10.1016/j.nantod.2014.09.004**.

49 Z. Yang, Z. Li, M. Xu, Y. Ma, J. Zhang, Y. Su, F. Gao, H. Wei and L. Zhang, *Micro Nano Lett.*, 2013, **35**(4), 247–259, DOI: **10.5101/nml.v5i4.p247-259**.

50 S. Zhu, Q. Meng, L. Wang, J. Zhang, Y. Song, H. Jin, K. Zhang, H. Sun, H. Wang and B. Yang, *Angew. Chem., Int. Ed.*, 2013, 3953–3957.

51 A. Das, V. Gude, D. Roy, T. Chatterjee, C. K. De and P. K. Mandal, *J. Phys. Chem. C*, 2017, **121**, 9634–9641.

52 A. Das, D. Roy, M. Mandal, C. Jaiswal, M. Ta and P. K. Mandal, *J. Phys. Chem. Lett.*, 2018, **9**, 5092–5099.

53 S. J. Cho, D. Maysinger, M. Jain, B. Röder, S. Hackbarth and F. M. Winnik, *Langmuir*, 2007, **23**, 1974–1980.

54 M. Wang, X. Lai, L. Shao and L. Li, *Int. J. Nanomed.*, 2018, **13**, 4445–4459, DOI: **10.2147/IJN.S170745**.

55 D. Segets, R. Marczak, S. Schäfer, C. Paula, J. F. Gnichwitz, A. Hirsch and W. Peukert, *ACS Nano*, 2011, **5**, 4658–4669.

56 Y. Braeken, S. Cheruku, A. Ethirajan and W. Maes, *Materials*, 2017, **10**(12), 1420, DOI: **10.3390/ma10121420**.

57 J. Manioudakis, F. Victoria, C. A. Thompson, L. Brown, M. Movsum, R. Lucifero and R. Naccache, *J. Mater. Chem. C*, 2019, **7**, 853–862.

58 G. F. Dawson and G. W. Halbert, *Pharm. Res.*, 2000, **17**, 1420–1425.

59 X. Huang, X. Teng, D. Chen, F. Tang and J. He, *Biomaterials*, 2010, **31**, 438–448.

60 B. Pelaz, P. del Pino, P. Maffre, R. Hartmann, M. Gallego, S. Rivera-Fernández, J. M. de la Fuente, G. U. Nienhaus and W. J. Parak, *ACS Nano*, 2015, **9**, 6996–7008.

61 M. Havrdova, K. Hola, J. Skopalik, K. Tomankova, M. Petr, K. Cepe, K. Polakova, J. Tucek, A. B. Bourlinos and R. Zboril, *Carbon N. Y.*, 2016, **99**, 238–248.

62 J. Rejman, V. Oberle, I. S. Zuhorn and D. Hoekstra, *Biochem. J.*, 2004, **377**, 159–169.

63 Y. Arezki, F. Delalande, C. Schaeffer-Reiss, S. Cianférani, M. Rapp, L. Lebeau, F. Pons and C. Ronzani, *Nanoscale*, 2022, **14**, 14695–14710.

64 M. Usman, Y. Zaheer, M. R. Younis, R. E. Demirdogen, S. Z. Hussain, Y. Sarwar, M. Rehman, W. S. Khan and A. Ihsan, *Colloids Interface Sci. Commun.*, 2020, 100243, DOI: **10.1016/j.colcom.2020.100243**.

65 N. Dhenadhayalan, K. C. Lin, R. Suresh and P. Ramamurthy, *J. Phys. Chem. C*, 2016, **120**, 1252–1261.

66 Y. Shu, J. Lu, Q.-X. Mao, R.-S. Song, X.-Y. Wang, X.-W. Chen and J.-H. Wang, *Carbon N. Y.*, 2017, **114**, 324–333.

67 T. V de Medeiros, A. Macina, J. P. de Mesquita and R. Naccache, *RSC Appl. Interfaces*, 2024, **1**, 86–97.

68 A. Clermont-Paquette, D.-A. Mendoza, A. Sadeghi, A. Piekny and R. Naccache, *Sensors*, 2023, **23**, 5200.

69 K. Holá, M. Sudolská, S. Kalytchuk, D. Nachtigallová, A. L. Rogach, M. Otyepka and R. Zbořil, *ACS Nano*, 2017, **11**, 12402–12410.

70 J. D. Roberts and M. Constance Caserio, *Basic Principles of Organic Chemistry*, W.A. Benjamin Inc., Menlo Park, 2nd edn., 1977.

71 S. dos Santos, B. Medronho, T. dos Santos and F. E. Antunes, in *Drug Delivery Systems: Advanced Technologies Potentially Applicable in Personalised Treatment*, ed. J. Coelho, Springer Netherlands, Dordrecht, 2013, pp. 35–85.

72 A. O. Adeola, A. Clermont-Paquette, A. Piekny and R. Naccache, *Nanotechnology*, 2023, **35**, 012001.

73 J.-R. Macairan, I. Zhang, A. Clermont-Paquette, R. Naccache and D. Maysinger, *Part. Part. Syst. Charact.*, 2020, **37**, 1900430.

74 J.-R. Macairan, D. B. Jaunky, A. Piekny and R. Naccache, *Nanoscale Adv.*, 2019, **1**, 105–113.

75 S. Salatin, S. Maleki Dizaj and A. Yari Khosroushahi, *Cell Biol. Int.*, 2015, **39**, 881–890.